Bioinspiration & Biomimetics

PAPER

A dynamical model exploring sensory integration in the insect central complex substructures

IOP Publishing Bioinspir. Biomim. 15 (2020) 026003 https://doi.org/10.1088/1748-3190/ab57b6

Bioinspiration & Biomimetics

RECEIVED
19 May 2019

REVISED
8 November 2019

ACCEPTED FOR PUBLICATION
14 November 2019

PUBLISHED
10 January 2020

PAPER

A dynamical model exploring sensory integration in the insect central complex substructures

S C Pickard[1], R D Quinn and N S Szczecinski

Department of Mechanical and Aerospace Engineering, Case Western Reserve University, Cleveland OH 44106, United States of America

[1] Author to whom any correspondence should be addressed.

E-mail: sxp671@case.edu

Keywords: central complex, sensory integration, spatial navigation

Abstract

It is imperative that an animal has the ability to contextually integrate received sensory information to formulate appropriate behavioral responses. Determining a body heading based on a multitude of ego-motion cues and visual landmarks is an example of such a task that requires this context dependent integration. The work presented here simulates a sensory integrator in the insect brain called the central complex (CX). Based on the architecture of the CX, we assembled a dynamical neural simulation of two structures called the protocerebral bridge (PB) and the ellipsoid body (EB). Using non-spiking neuronal dynamics, our simulation was able to recreate *in vivo* neuronal behavior such as correlating body rotation direction and speed to activity bumps within the EB as well as updating the believed heading with quick secondary system updates. With this model, we performed sensitivity analysis of certain neuronal parameters as a possible means to control multi-system gains during sensory integration. We found that modulation of synapses in the memory network and EB inhibition are two possible mechanisms in which a sensory system could affect the memory stability and gain of another input, respectively. This model serves as an exploration in network design for integrating simultaneous idiothetic and allothetic cues in the task of body tracking and determining contextually dependent behavioral outputs.

1. Introduction

As roboticists, we hope to one day construct robots that can complete tasks autonomously, adaptively, and in a truly intelligent fashion. To design such a control system, our work looks to the abilities of animals as inspiration—specifically insects, whose nervous systems may be more tractable than those of vertebrates—and to understand the neurological underpinnings of these abilities. Of particular interest to us is how animals are able to employ many sensor types and integrate their inputs seamlessly within the brain. One such task that requires multimodal inputs (and will serve as a proof-of-concept task within this paper) is the ability to track body position within the environment. The work presented here simulates the experimental setup of Varga and Ritzmann where a rotating platform is able to induce rotational cues in an animal that is fixed to the turntable [1]. In the simulation, when the table rotates, idiothetic updates are detected by approximated chordotonal stretch sensors at the base of the antennae and relayed to a biologically-inspired sensory integrator responsible for tracking body heading. Although the connectivity and dynamical behavior of this integrator are not fully mapped or understood, neurobiology has offered insight into the brain substructures that appear to play a pivotal role in this task [1–6].

A region of great interest to neurobiologists is a structure known as the central complex (CX). The CX is a midline brain structure found in all arthropods [7] and in most species, it is comprised of four neuropils: the protocerebral bridge (PB), the fan shaped body (FB), the ellipsoid body (EB), and the noduli [7–9]. Wolff *et al* contributed an excellent survey of CX connectivity that showed a richly complex network between the PB, FB and EB, and although Wolff's paper does not address functional roles of the cell types, it provides a detailed framework for the 'wiring rules' of these neuropils [9].

CX mutant and lesion studies found this brain region to be pivotal in sensory integration [6, 10–13] and neuromodulation for adaptive output behaviors such as flight [14, 15], walking [12, 16, 17], turning

[18, 19], and navigation [20, 21]. Recent optogenetic studies have shown the participation of the CX in navigational tasks, where a two photon calcium imaging technique enables researchers to monitor population activity of genetically manipulated neurons within the CX while the animal is walking and visually engaged with virtual landmark inputs [22]. From these studies, populations of neurons within the EB showed correlative activity to body rotational position and landmark cues. Building on these experiments, studies into the neuronal architecture of the CX determined a well structured connectivity and coordinated activity between the PB and EB [2, 4]. Specifically, a recursive excitatory connectivity between the eight P-EN cell populations of the PB (PB_{G2-9}.s-EBt.b-NO_1.b [9]) and the eight E-PG tile cell populations of the EB (PB_{G1-8}.b-EBw.s-D/Vgall.b [9]) maintain activity correlated to body heading and speed. In brief, activity is initiated in the EB ring by input currents from rotational sensors and due to the internal inhibition networks of the EB, a unimodal distribution of electrical activity emerges, dubbed the 'bump' activity. This bump activity is able to oscillate about the EB ring and corresponds to the animal's heading [2, 4, 23].

If this bump activity seen in the EB is the brain's representation of the body's heading, how might multiple sensory systems that give analogous information about the true heading be integrated by the brain to produce this believed position? For instance, if chordotonal antennal inputs as well as visual inputs can both provide ego-motion cues, how might the brain combine these input signals to finalize the perceived body position? Experimentation from Kim *et al* and Green *et al* both give insight to this question of position updates through the use of artificial stimulations deployed in the EB and the PB, respectively [2, 24]. Kim *et al* explored how direct photon stimulation to various EB tiles can cause quick updates to believed body position, or 'bump jumps', within the EB. This causes the locus of activity to quickly jump without continuous flow through sequential tiles [24]. Related to this, Green *et al* induced bump jumps within the E-PG populations from targeted P-EN ATP injections [2]. These studies provided inspiration for several simulated experiments in our work, wherein sensory information from a more reliable sensory input could cause a 'bump jump' to the correct orientation and offset accumulated error from different sensory inputs.

Several recent models have sought to reproduce and explain the dynamics of the CX, to explore how this brain region may give rise to navigational abilities [3, 25–31]. Like the work presented here, these models present a similar biologically-constrained connectivity and use dynamical neural components to reproduce key features of the CX. Although there is similarity across the connectivities of the models, the questions being asked by the respective groups are unique. In this paper, we pose a question about the relevance of the bump width. Specifically, does the width of the bump change and if so, is it a proxy for certitude in the determined heading? We ask this question because in the field of robotics, probabilistic algorithms are used to combine noisy readings from multiple sensor types (such as the antennal *and* visual inputs mentioned above), compare said sensory inputs with approximate kinematic models, and output a single predicted heading. The similarities to this Bayesian algorithmic approach to sensory integration and neural integration have been suggested in mammals as well as arthropods [32, 33]. If such similarities prove true, does the CX contextually integrate inputs and give more weight to trusted modalities?

In this paper, we first show that the biologically-inspired connectivity [2, 4, 9] in combination with neuronal dynamics, is sufficient in reproducing *in vivo* CX behavior for a rotating body in the yaw plane. By reproducing these behaviors [2, 4], we hope to establish a credible simulation framework for the basic mechanisms of the PB-EB communications. In summary, four behaviors of the CX that we are able to reproduce in simulation include:

1. The direction of body rotation dictates the activity bump's direction of motion in the EB layer.
2. The body's rotational speed correlates to bump activity speed in the EB.
3. The heading, determined by peak bump activity, can be updated with artificial stimulation applied to an EB neuron population, thereby causing a 'bump jump'.
4. A 'bump jump' can be induced through artificial stimulation applied to the PB neuronal populations as well.

Subsequently, we present several potential mechanisms by which real time gain modulation of competing sensory inputs can be integrated asymmetrically *at the level of the CX*. We aim to show that through plasticity in EB memory connections and internal inhibitory connections, the width of the activity bump can be controlled, thereby encoding the variance of the EB's believed body orientation. When mapping output motor commands to the efferent pathways, this modulated EB projection can relay both the determined body heading and the level of certainty in which this heading is believed to be true.

2. Methods

2.1. Self-motion detection with chordotonal sensors

We constructed a model in Animatlab, a 3D graphics environment for neuromechanical simulations [34], to simulate an agent on a rotating platform. Our simulation setup is a reproduction of a Varga and Ritzmann experiment aimed at assessing the interplay of visual and chordotonal inputs within the CX of a

fixed animal on a turntable [1]. During the experiment performed by Varga, the animal's head was covered in foil, eliminating visual input and presumably reducing wind input [1]. We assumed that the primary idiothetic sensory modality available to detect motion would be the stretch of chordotonal organs (COs), specifically Johnston's organs, in the base of the antennae. The CO stretch would signify rotational acceleration and steady-state rotational velocity, much like an inertial measurement unit [35–41].

In the simulation environment, we reproduced this rotational platform with a fixed body and antennae setup which served as a dynamically responsive sensor to rotational cues (figures 1(A) and (B)).The antennae were modeled as critically damped mass-spring-damper systems (figure 1(C)) and serve as a means to detect rotational velocity. Each antenna converted the positive elongation of the spring (i.e. the CO) to current input to a sensory neuron [42]. Thus, as the circular platform experienced rotational acceleration, one CO would stretch and induce current into its sensory neuron while the other compressed and did not induce current into its sensory neuron, yielding an asymmetrical response. These two sensory neurons mutually inhibit one another to form a bistable network. This bistable network is necessary because once the disk is spinning at a constant, steady-state angular velocity, both antennae will be deflected symmetrically toward the midline of the body due to centrifugal force, with no net neural activation. However, the bistable network ensures that whichever CO relaxed during acceleration is silenced by the CO that stretched, enabling an asymmetrical *neural* response from the symmetrical *mechanical* response.

The mechanical stimulus is then linearly mapped to an electrical current value, I_{app}, that is injected into the CX as will be discussed in section 2.3. The transfer function that maps the chordotonal stretch to a current [43] is given by

$$I_{app} = R \cdot \frac{\theta - \theta_{min}}{\theta_{max} - \theta_{min}}, \tag{1}$$

where θ is the sensory input and R is the user-defined functional range of the sensory neuron (defined here to be -0.06 V to -0.04 V). This mapping function has great utility when considering that any sensor with a characteristic operational range could be mapped to the sensory neurons. Parameters for the sensor can be calculated from the fundamental equations of rotational motion provided in appendix A.1.

2.2. Neurons are modeled as leaky integrators

1 The neurons were modeled with linear conductance dynamics [43] to represent time dependent electrical properties. The voltage of the postsynpatic neuron above rest has the dynamics

$$C_{mem}\frac{dV}{dt} = I_{Leak} + I_{syn} + I_{app}. \tag{2}$$

Equation (2) states that the change of the membrane voltage V times the capacitance of the membrane C_{mem} (left hand side) is equal to the total current across the cell membrane (right hand side). The total current is made up of the incoming, applied current I_{app}, plus the current due to ion flux through membrane gates, I_{Leak}, plus the current across the synapse (transmitter induced), I_{syn}. Substituting current equations (3) and (4) into (2), gives the form seen in equation (5)

$$I_{Leak} = G_{mem} \cdot (E_{rest} - V) \tag{3}$$

$$I_{Syn} = g_{syn} \cdot (E_{syn} - V) \tag{4}$$

$$C_{mem}\frac{dV}{dt} = G_{mem} \cdot (E_{rest} - V) + g_{syn} \cdot (E_{syn} - V) + I_{app}, \tag{5}$$

where G_{mem} is the constant membrane conductance, E_{rest} is the equilibrium potential constant (voltage where inward and outward currents are equal), E_{Syn} is the reversal potential of the synapse (sets the minimum postsynaptic neuron voltage activity), and g_{syn} is the varying conductance of the synapse dependent on the activity of the presynaptic neuron as follows:

$$g_{syn} = G_{syn_{max}} \cdot \begin{cases} 0 & \text{if } V_{pre} < E_{rest} \\ \frac{V_{pre} - E_{rest}}{E_{high} - E_{rest}} & \text{if } E_{rest} \leqslant V_{pre} \leqslant E_{high}. \\ 1 & \text{if } V_{pre} > E_{high} \end{cases}$$

Here, E_{high} represents the upper bound of activity. The synaptic conductance saturates for any voltage activity exceeding this value. Taken together, E_{rest} and E_{high} define the functional range of the postsynaptic neuron [43].

2.3. *In silico* neuron connectivity

The dynamical neural model of the CX was constructed in Animatlab to work in conjunction with the mechanical stimulus of the turning disk and the antennal chordotonal sensor discussed in section 2.1.

We constructed a neuron-to-neuron connectivity representative of the observed recursive excitatory connectivity between the PB and EB (figure 2), where each neuron is modeled with the leaky integrator dynamics discussed in section 2.2. This schematic represents the assembly of the processing layers of our simulation while remaining representative of *in vivo* neuronal connectivity. As seen in figure 2(A), the P-EN cell type have their dendritic inputs located in the PB [9], where they receive inhibition signaling from the lateral interneurons, while their axonal outputs extend to the EB to articulate bilaterally with E-PG networks [2]. After receiving inputs from the P-ENs, the E-PGs have their axonal projections terminate in the PB and communicate with the adjacent column of P-ENs—thereby moving the activity to the adjacent column [2, 4, 9]. Extrapolating the connectivity seen in literature, two cell types and an internal EB inhibition network were required for proper activity. While

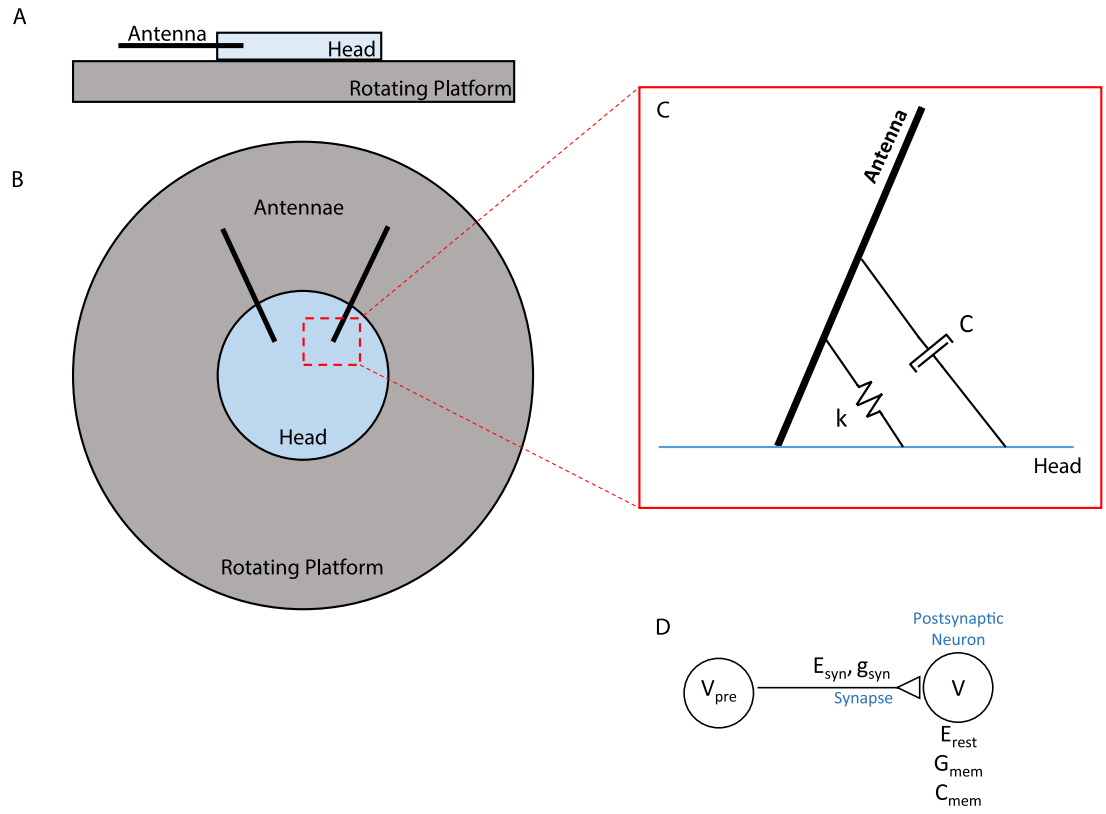

Figure 1. Antennae chordotonal sensors. The antennae were modeled as mass spring-damper systems (one for each antenna) to serve as the rotational velocity detectors. The deflection of the antennae (mass bar) generates a proportional current in the simulation setting. This is injected into the CX via the disinhibitory mechanism through the PB. Side view (A) and top view (B) of platform setup in simulation setting. (C) A zoomed in view of the antennal mass spring-damper system for a single antenna. (D) Neuron-to-neuron connection showing where parameters apply.

constructing the simulation, certain assumptions were employed in order to produce the dynamics seen in animals.

First, the lateral interneurons (figure 2(A)) are situated such that while active, these cells are able to inhibit their respective side of the PB-EB axis proportionally to the degree of their activity. These lateral interneurons function in a tonic mode until they are hyperpolarized by chordotonal sensor currents thus permitting the P-ENs to be depolarized and participate in the EB/PB communication loop. Second, autaptic disinhibitory connections of the E-PGs form memory networks (figure 2(B)) that are required for long term memory (i.e. persistent bump activity) when the body is at standstill [43], as well as coordinating network oscillatory activity while the body is in motion. Third, the internal inhibition of the EB comes into play when the activity of a single E-PG causes hyperpolarization of all other E-PGs except those immediately adjacent (figure 2(B)). This mechanism permits the localized maximal activity—the bump—and prevents ambiguity of multiple peaks within the EB.

2.4. Tuning network parameters

These equations contain many parameter values that must be tuned. Using developed methods for selecting parameter values based on the function of network components [43], we were able to assemble a network whose overall behavior satisfied our goals in section 1. Thus, we created a dynamical neural model of the 'bump handoff' using known neuroanatomy and our functional subnetwork approach. Using this approach, we can assign functional roles to the neuron populations of EB/PB axis to have them perform specific signal modulation operations. Figure 2(C) shows a simplified functional representation of our CX model.

Lateral interneurons in the PB modulate the conductance and therefore, the sensitivity of all P-EN cells in one half of the PB. The parameter values of these lateral interneurons allow them to act as a multiplication network that controls the level of disinhibition of the P-EN cell populations [43]. That is, the current received from the stretching of the antennal CO is able to modulate the gain of the E-PG-to-E-PG signal transmission through this interneuron multiplication subnetwork. Modelling the P-ENs as an addition subnetwork, the P-ENs act to positively feedback the incoming activity of the connecting E-PGs, in the excitatory recursive loop. With the functional subnetwork calculations, we know that each P-EN's steady state voltage is approximately

$$V_{\text{P-EN},n} = E_{\text{rest}} + V_{sensory} \cdot \frac{V_{\text{E-PG},n} - E_{\text{rest}}}{E_{\text{high}} - E_{lo}}. \quad (6)$$

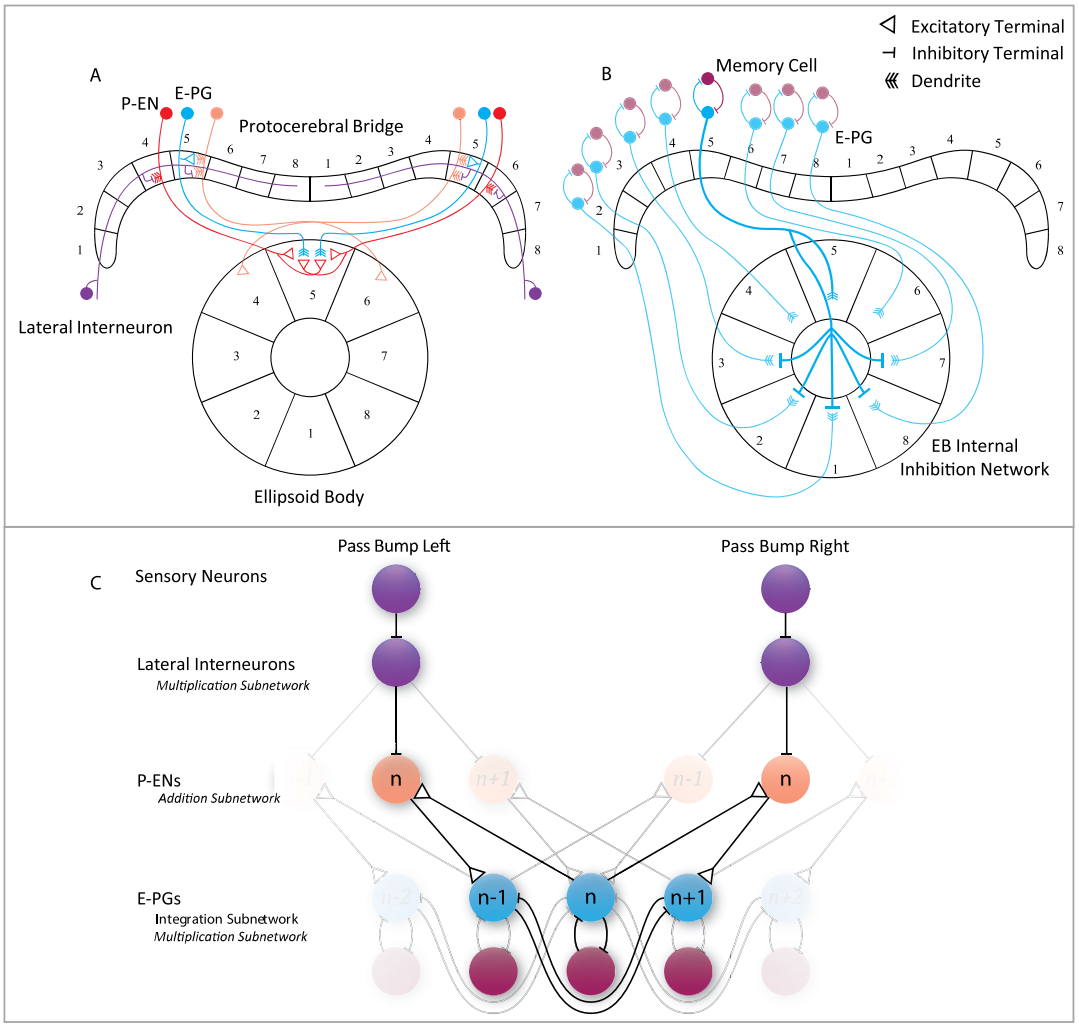

Figure 2. Connectivity. (A) The loci of dendrites and termini of P-EN and E-PG cells within the EB and PB. The lateral interneuron runs through the PB, where it receives inputs from chordotonal sensors (not shown) and outputs inhibitory control of same-side P-ENs. (B) The memory cells form an inhibitory recursive connection with the E-PG cells. The internal inhibitory network is formed when the terminus of an E-PG articulates with the dendrites of E-PGs in the EB except the immediate bilateral neighbors (example connectivity where only one E-PG inhibitory network is shown). (C) Diagram showing the functional connectivity networks of our CX model. E-PG$_n$ projects to the PB via the right and left P-EN$_n$. These neurons then project down to E-PG$_{n+1}$ and E-PG$_{n-1}$, respectively, and act as an excitatory transmission (addition network). The excitability of the P-ENs, and thus the gain of the recurrent excitation, is controlled by the sensory neurons, each of which disinhibit all P-ENs on one side of the PB through their respective lateral interneurons (multiplier network). This changes the gain with which the bump is passed to the right or left in the EB, and therefore the speed and direction of the bump. The memory functionality of the E-PGs allows for sustained tile activity, even while body rotation has stopped (integration network).

In our model, the E-PG cells are memory units (i.e. non-leaky integrators) that maintain persistent bump activity (even when no external stimulus is present) and are modelled as an integrator subnetwork. Within the modeled EB, there is an interconnected multiplication network of the E-PG tiles that when a single tile is active, it can modulate the sensitivity of all other E-PG populations (except for immediate neighbors). This inhibition network between tiles ensures that after the bump is passed to a new tile, the previous tile is inhibited and becomes silent. If the body is experiencing left-hand rotation, for instance, the EB will experience a right-hand 'pass bump' from E-PG cell n to $n+1$ with the approximate voltage response over time of

$$V_{\text{E-PG},n+1} = \int k_i \cdot \frac{V_{\text{P-EN},n} - E_{\text{rest}}}{E_{\text{high}} - E_{lo}} \cdot dt, \qquad (7)$$

the constant k_i depends on the capacitance of the E-PG neurons [43].

Most parameters seen in table 1 were calculated using equations (6) and (7), which are applications of the functional subnetwork approach [43]. However, to get accurate EB localization, the integration constant k_i needed to be designed to map the disk's rotational velocity with the EB bump's angular velocity. We used Newton's method [44] for constrained optimization to tune the neuronal time constants of both the E-PG and memory cell populations such that the resultant body direction vector can be calculated accurately from the bump activity within the EB. Newton's method is an iterative approach that attempts to converge to an optimum solution, i.e. a set of values for the E-PG and memory cell time constants. Note that this

Table 1. Parameter value summary: most values were calculated using the subnetwork approach introduced in [43], however, to get accurate EB position determinations, the neuronal time constants, $\tau_{\text{E-PG}}$ and τ_{Memory} were tuned using a nonlinear optimization solver. A constraint we imposed on the network was that these two neuron types were to have the same time constant. LI: lateral interneuron; E_{syn} = reversal potential of the synapse, g_{syn} = maximum conductance of the synapse.

Parameter	Calculation source	Value
LI τ	[43]	0.05 s
P-EN τ	[43]	0.05 s
E-PG τ	Optimization	0.012 178 s
Memory τ	Optimization	0.012 178 s
LI:P-EN E_{syn}, g_{syn}	[43]	−0.061 115 V, 20 μs
P-EN:E-PG E_{syn}, g_{syn}	[43]	0.134 V, 115 ns
E-PG:P-EN E_{syn}, g_{syn}	[43]	0.134 V, 115 ns
E-PG:Memory E_{syn}, g_{syn}	[43]	−0.1 V, 0.5 μs
Memory:E-PG E_{syn}, g_{syn}	[43]	−0.1 V, 0.5 μs
E-PG:E-PG E_{syn}, g_{syn}	[43]	−0.06 V, 0.5 μs

method can converge to *a* solution and not necessarily the *best* solution. The constraint functions mentioned are those functions that direct the optimization technique towards the goal of interest. In this case, our goal was to find the E-PG and memory cell time constant values that minimized the mean squared error of the disk rotation to the bump rotation within the EB, thereby giving a one-to-one matching in rotation of the turntable platform to the rotation of the bump in the EB. In other words, when the turntable (on which our simulated insect is fixed) induces one physical turn of the body, the EB bump will also make a single full rotation within the EB. We found the time constants of the E-PG and memory cells greatly affected the timing in which the bump moved about the EB, so in lieu of attempting to optimize the entire EB/PB model parameters (which would be several dozen parameters assuming symmetry), we decided to just tune these neuron types. The calculated values for these neuron time constants that allowed this one-to-one turn ratio are reported in table 1.

3. Results

3.1. *In silico* model emulates *in vivo* behavior

3.1.1. Direction of body rotation dictates direction of EB bump activity

The PB/EB network was designed to follow observed CX behavior such that when the simulated body experiences counterclockwise motion in the yaw plane, the PB and EB activity bumps move clockwise (figures 3(A)–(C)); the opposite is true for clockwise body motion causing counterclockwise bump activity in the PB and EB. (figures 3(D)–(F)) [2, 4]. Within the simulation, side biasing occurs when sensory neurons from the COs at the base of the antennae have asymmetrical responses to the rotational acceleration. These CO inputs directly modulate the lateral interneurons and cause side-selective disinhibition of the PB. The connectivity is such that when the P-ENs of the preferred side of the PB are disinhibited relative to the non-preferred side, the sustained neuronal activity in the EB is able to transmit from the E-PGs to the P-ENs residing in the preferred side of the PB. Once the preferred side P-ENs depolarize, it is the recursive excitatory loop that transmits the activity from these P-ENs back to the E-PGs that are shifted either one tile in the clockwise direction (for P-ENs from the left PB) or counterclockwise (for P-ENs from the right PB). When the body accelerates in the other direction, the chordotonal sensors quickly detect this directional change, resulting in a reversal of lateral interneuron inhibition proportionality and side biasing. When the bilateral antennae sensors experience symmetrical deflection, it is interpreted as no body rotation. This would result in a stationary peak within the EB corresponding to the real-time translational heading, and would be maintained indefinitely until body rotation recommences.

3.1.2. Body rotation speed dictates EB bump activity speed

When the body rotates at a faster speed, the chordotonal sensor stretches to a greater extent (while the other relaxes), causing a larger hyperpolarizing current directed to the corresponding lateral interneuron. The preferred side P-ENs are more disinhibited and with that, comes the ability to depolarize faster and to a greater magnitude. For a distinct unilateral chordotonal input as seen in figure 3, there is a clear preferred side (right P-ENs; figure 3(H)) that has a larger depolarization magnitude and decreased rise-time (steeper slope) with increasing speed, while the non-preferred side shows minimal activity (figure 3(I); note the voltage value differences as compared to the other y-axes). The resulting asymmetric activity of the P-ENs of the preferred versus non-preferred side keep the signal side biased and correlated to the body's speed and direction.

The EB bump profiles (figure 3(I)) show that the E-PGs depolarize to roughly the same degree with an all-or-nothing activity during body motion; however, faster depolarization is seen with faster body rotational speed.

3.1.3. Artificial stimulation in neuropils can cause bump jumps

To quantify the necessary artificial stimulation necessary to instigate a bump jump within our simulation environment, the artificial stimulation was modeled as a tonic applied current injected into cell populations at the level of the PB (P-ENs only) or E-PGs of the EB. By setting the current amplitude, duration, and locus of injected populations, we quantified what necessary stimuli are needed to instigate a bump jump for a stationary body or for a body undergoing rotational motion.

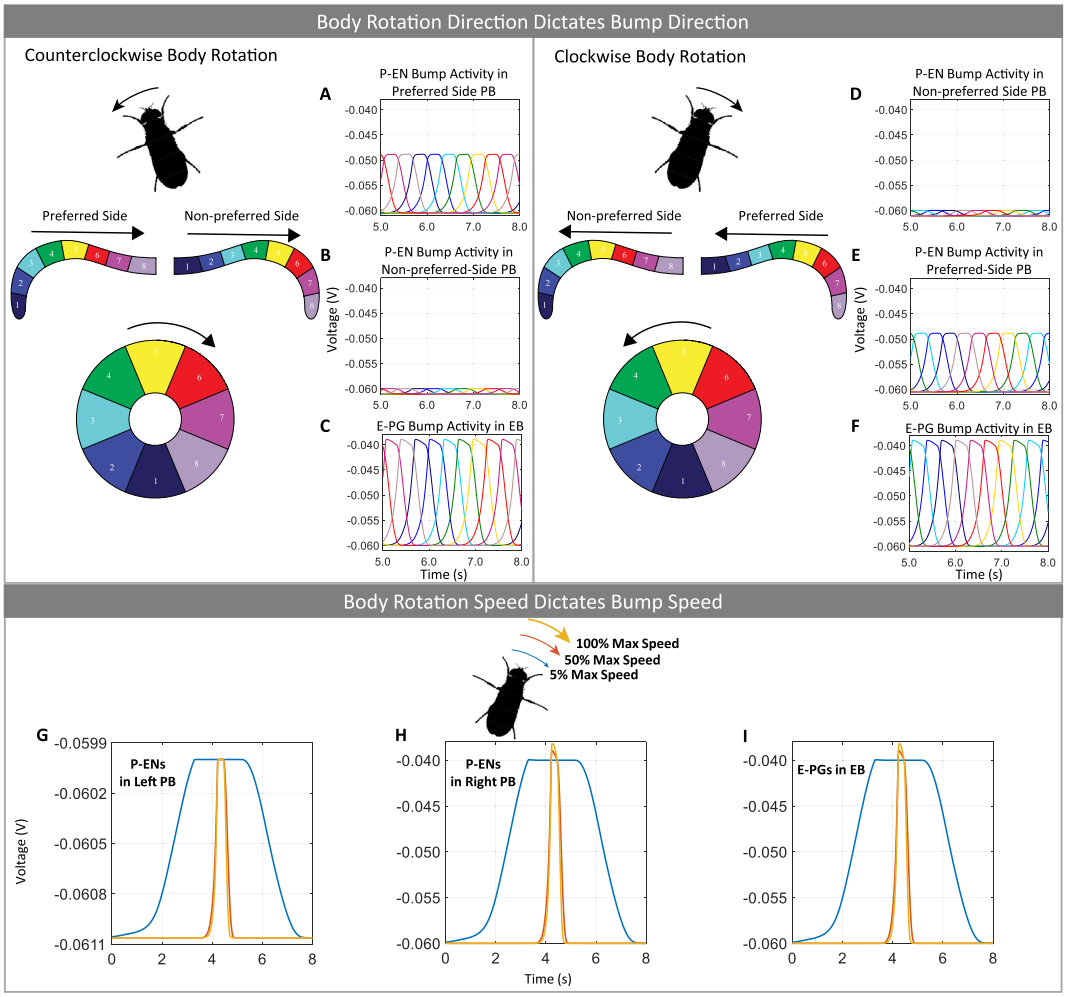

Figure 3. Body direction and rotational speed dictates direction and speed of bump activity in P-ENs and EB. TOP: the glomeruli of the PB and the tiles of the EB are color coded to the time varying voltage bumps seen in the graphs. Graphs (A)–(C) correspond to left-hand body rotation where (A) shows the preferred side P-ENs have larger depolarization magnitudes than seen in (B), the non-preferred, right P-ENs. (C) The E-PGs, like the P-ENs in both (A) and (B), has right-hand bump activity. Graphs (D)–(F) correspond to right-hand body rotation, where now all graphs show left-hand bump movement. However, with the directional change in body rotation, the PB non-preferred side is now (D) the left while the preferred is (E) the right. BOTTOM: right hand body rotation at varying speeds produces variation in the bump profiles of the PB and EB. (G) The non-preferred side P-ENs show a slight depolarization saturation level and a rise-time (slope) that does not appear to correlate strongly to speed. The preferred side P-ENs (H) shows a strong correlation of depolarization magnitude and rise-time to that of body speed. (I) The E-PGs of the EB have an all-or-nothing activity during body motion, where depolarization always reaches the saturation level of −0.04 V.

Artificial stimulation in a stationary body

The stationary body simulation is initialized by allowing the body to rotate at constant angular velocity for 4 s and then brought to a standstill. This initialization step establishes the t_0 body heading (denoted as the 'original bump' in the figures) prior to applying the artificial stimulations. At this time, a depolarizing current was either applied to the E-PGs at the offset locus within the EB or to the appropriate P-EN to cause the same shift within the EB. Immediate E-PG neighbors to a tile are located at this 45° offset location and because immediate neighbors do not inhibit one another, the artificial stimulations implemented at this close proximity causes a greater spread in activity and not a bump jump (figures 4(B) and 5(B)). Artificial stimulation applied directly to the EB at a 90° or a 180° offset requires a large current amplitude of at least 50 nA to successfully cause a bump jump for a short stimulus duration of 0.01 s (figures 4(C) and (D)). Smaller amplitudes were able to cause direct EB stimulated bump jumps when the duration was increased, sometimes requiring 3 s to successfully alter the locus of activity (figure 4(D)). Stimulation through the PB, in general, required a greater stimulus magnitude and longer duration to elicit a bump jump, with even the greatest magnitude tested (100 nA) requiring 0.1 s (figures 5(C) and (D)).

Artificial stimulation in a rotating body

When the body is rotating, maintaining rotational accuracy also becomes a factor during the artificial stimulations. With a body rotation of 2π rad s^{-1}, we calculated a peak-to-peak time (the time it takes for maximal bump activity to move from one tile to the next) of $t = 0.1260$ s. To test the feasibility of bump jumps in an EB that has moving activity, this peak-

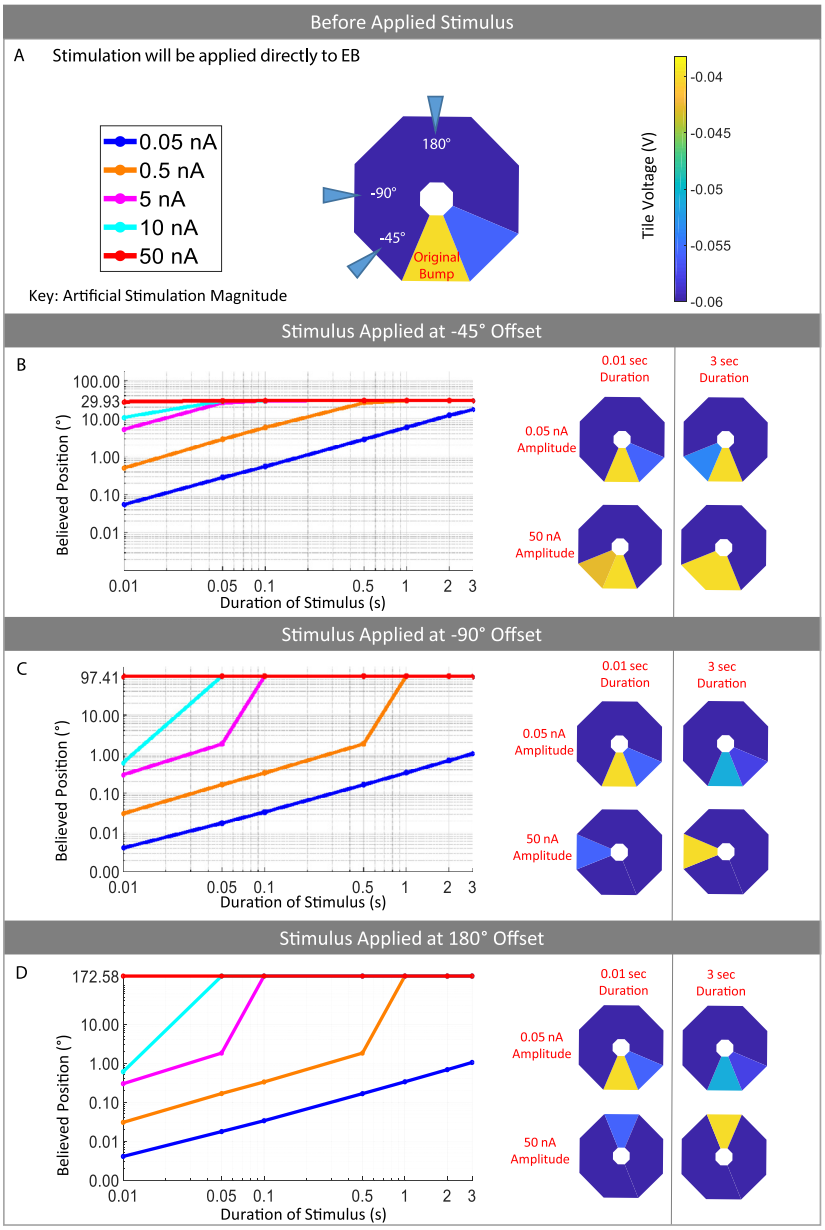

Figure 4. Artificial stimulations applied directly to the EB cause bump jumps while the body is stationary. Prior to the application of the artificial stimulation, the original bump location is shown on the octagonal plots (A). Additionally, this plot shows where the artificial stimulation is applied at −45°, −90°, and then 180° offsets from the original bump location. Octagonal plots for (B)–(D) show examples of resulting activity in the EB following the implementation of the artificial stimulation. (B) No 45° stimulations were able to cause a bump jump. Successful 90° and 180° bump jumps required a stimulation with an amplitude of at least 50 nA for fast (0.01 s) jumps (C) and (D). Note that 100 and 75 nA is superimposed with 50 nA curves. Smaller amplitudes of 10, 5, and 0.5 nA were successful but required longer stimulus durations.

to-peak time was used for all artificial stimulation durations but varied in locus and amplitude. Again, a locus of 45° did not cause a bump jump for either stimulation directly to the EB or to the PB (figures 6(A) and (D)). Both 90° and 180° shifts caused bump jumps for larger stimulation amplitudes only when directly induced through the EB. In our simulation, we were unable to get bump jumps with stimulations 100 nA or below when applied to the PB (figures 6(E) and (F)). With a moving body and thus transient tile activity, it became more difficult to have even high amplitude stimulation override the motion-induced EB activity. As an example, 100 nA at a 180° offset only instigated a reduction in bump activity magnitude and not a complete change in locus (figure 6(F)). Higher stimulation amplitudes with the constant time duration of $t = 0.1260$ s were successful but required magnitudes of around 200 nA to induce bump jumps (not shown). Longer time duration with 100 nA or below was successful, however, timing became an issue when the duration exceeded the peak-to-peak time.

3.2. CX behavior that emerges from simulation

3.2.1. Loss of EB coherence with direct network stimulation

Although our simulation was able to reproduce EB bump jumps seen in Kim *et al*, we found a scenario in which an artificial stimulation deployed directly

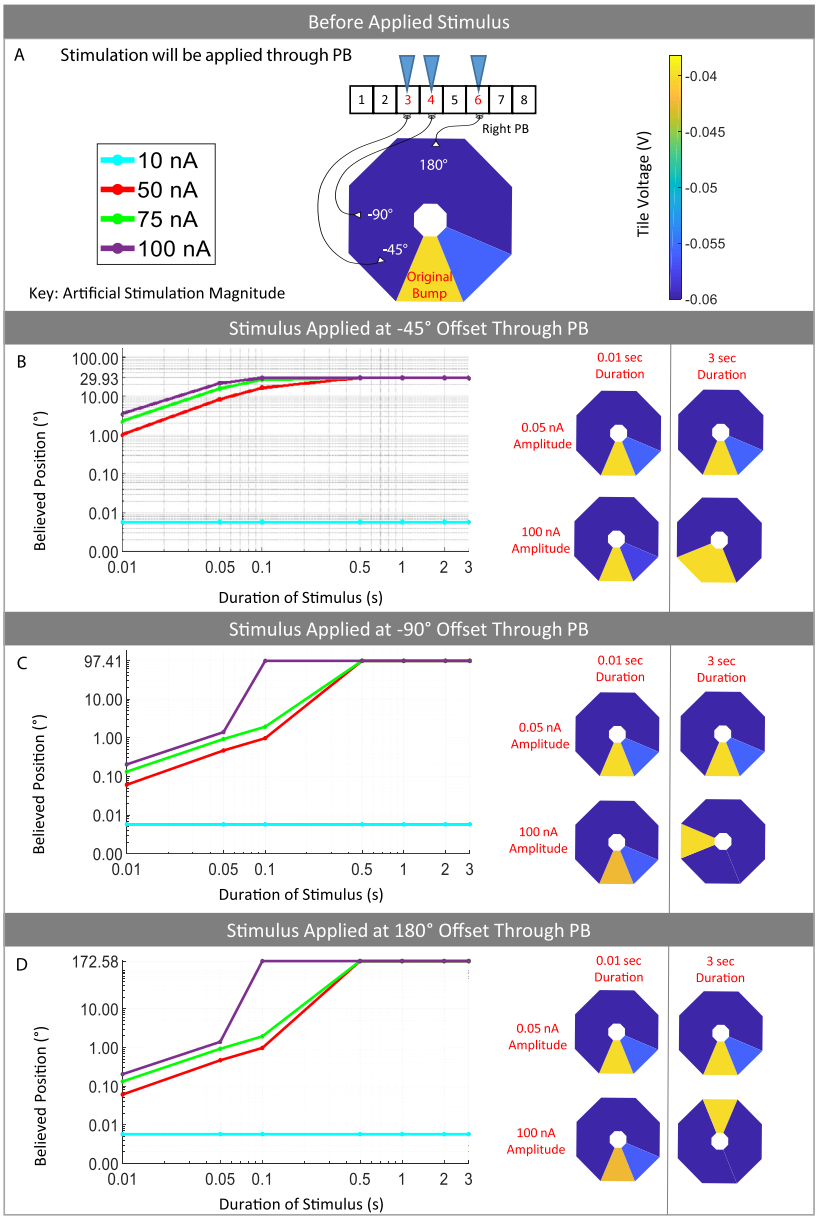

Figure 5. Artificial stimulations applied through the PB cause bump jumps in EB while the body is stationary. (A) EB activity prior to stimulus. (B) No 45° stimulations were able to cause a bump jump. Successful 90° and 180° bump jumps required a stimulation with an amplitude of at least 50 nA. Even with longer durations, stimuli below 50 nA did not elicit a bump jump.

to an E-PG population resulted in the loss of EB coherence (figure 7). A 0.08 s, 10 nA tonic stimulation applied to the 180° offset E-PG population caused a partial increase in depolarization at that shifted locus but a failure to maintain the increased activity, with complete bump activity collapse after ~0.20 s following the applied stimulus (figures 7(A), (B) and (E)). This results in the model totally losing track of the believed orientation of the body.

3.2.2. *Effects of EB internal inhibition tuning*

The internal inhibition network of the EB is the result of each E-PG making inhibitory connections to all other tiles. When a single E-PG is active, it is able to silence other tiles so as to maintain a single activity bump within the EB. However, the activity bump needs to be passed from this active tile to its immediate neighbor, and so to avoid simultaneous tile depolarization/hyperpolarization, immediate neighbors are not inhibited in our simulated network. The aim of this experiment was to explore how the synaptic reversal potential, E_{syn}, and the synapse conductance, g_{syn} of all internal inhibitory connections, affected the overall bump activity behavior of the EB.

The parameter values of the inhibition network greatly impacted the bump speed within the EB (given a particular body rotation speed) as well as the polar variance [45] of tile activity. The speed of the EB bump activity was seen to increase with increasing synapse conductance while the effect of the reversal potential was at its minimum of −0.06 V (figure 8(A)). The activity polar variance (i.e. the number tiles that participate in the activity bump at any given time) shows the inverse trend, where a decreasing polar variance

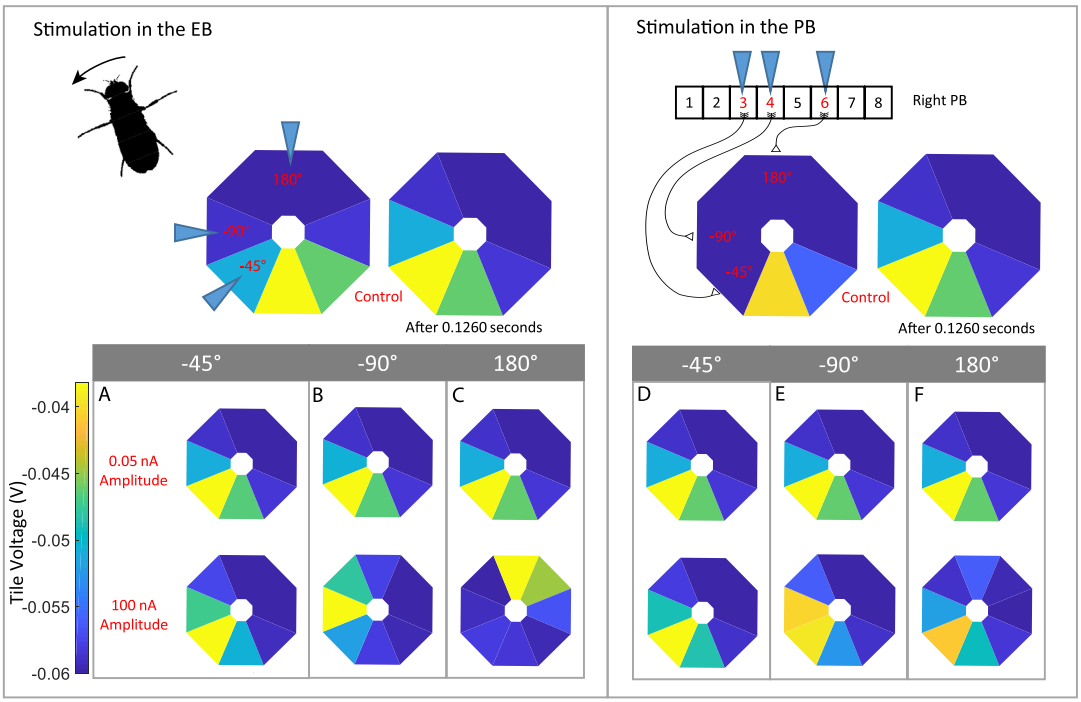

Figure 6. Artificial stimulations have less success in causing bump jumps in EB of a moving body. (A) and (D) A −45° offset was unable to cause a bump jump regardless if the artificial stimulation was applied to the EB or PB. (B) and (C) A −90° and 180° offset applied in the EB was able to cause a shift in believed position for larger amplitudes. (E) and (F) A −90° and 180° offset applied through the PB was unable to cause a bump jump up to 100 nA.

is seen with increasing synapse conductance (figures 8(B) and (C)). The E_{syn} parameter produces very similar profiles for $E_{syn} = -0.07$ V or less (more negative).

Both the speed and polar variance profile for $E_{syn} = -0.06$ V are strikingly different: first, the speed gradually increases with increasing conductance, while more negative E_{syn} profiles show rapid increases (figure 8(A)). Secondly, $E_{syn} = -0.06$ V produces a similar polar variance profile, but like its corresponding speed profile, it functions within a larger range of conductance values g_{syn} (figure 8(B)).

3.2.3. *Effects of memory synapse tuning*

The memory cells form a recursive inhibitory connection with the E-PGs and serve as the memory mechanism to this network. The design of this recursive inhibitory connection generates a resultant excitatory effect necessary to counteract the leak current that the E-PGs would otherwise experience (see [43] for a more thorough discussion of memory cells). The counteracting excitatory current is designed to permit persistent activity in the network even when applied current is removed, thus serving as a memory mechanism. We explored various design approaches to this memory network (figure 9) to show different types of memory that can be created simply by tuning the parameters. By keeping $E_{syn} = -0.1$ V constant, the controlling parameter becomes the conductance of the synapse, where three functional regimes emerged (figures 9(A)–(C)). In this simulated experiment, the body experiences rotational motion and then is brought to a standstill (i.e. CO sensory neuron current input ceases). Depending on the E_{syn}/ g_{syn} values of the memory synapses, the residual EB activity shows a specific type of memory trace following the stop in body motion. The first regime can be described as memory decay (figure 9(A)) where the memory trace loses amplitude with time. The rate of the decay can be modulated very finely by changing the conductance value (figure 9(A) top versus bottom).

Sustained memory is a persistent tile activity with constant amplitude that will only change when the body recommences rotation. Because the amplitude of the active tiles remains constant indefinitely, the perceived body position remains constant until a change in body position alters the change in tile activity. In our simulation, this sustained memory regime occurs at a conductance value of $g_{syn} = 0.50\ \mu$s (figure 9(B)).

Saturated activity occurs at values slightly above the sustained activity conductance value and can be described as a saturation to the upper bound of permitted tile activity. For tiles with activity above a threshold at the time of stop, a complete saturation to maximal activity of −0.04 V is seen. For tiles below this threshold at the time of stop, the tile activity goes to the rest potential of −0.06 V (figure 9(C)).

4. Discussion

In this paper, we presented a simulation of the CX that aims to explore potential mechanisms for multimodal integration of sensory inputs. We approximated

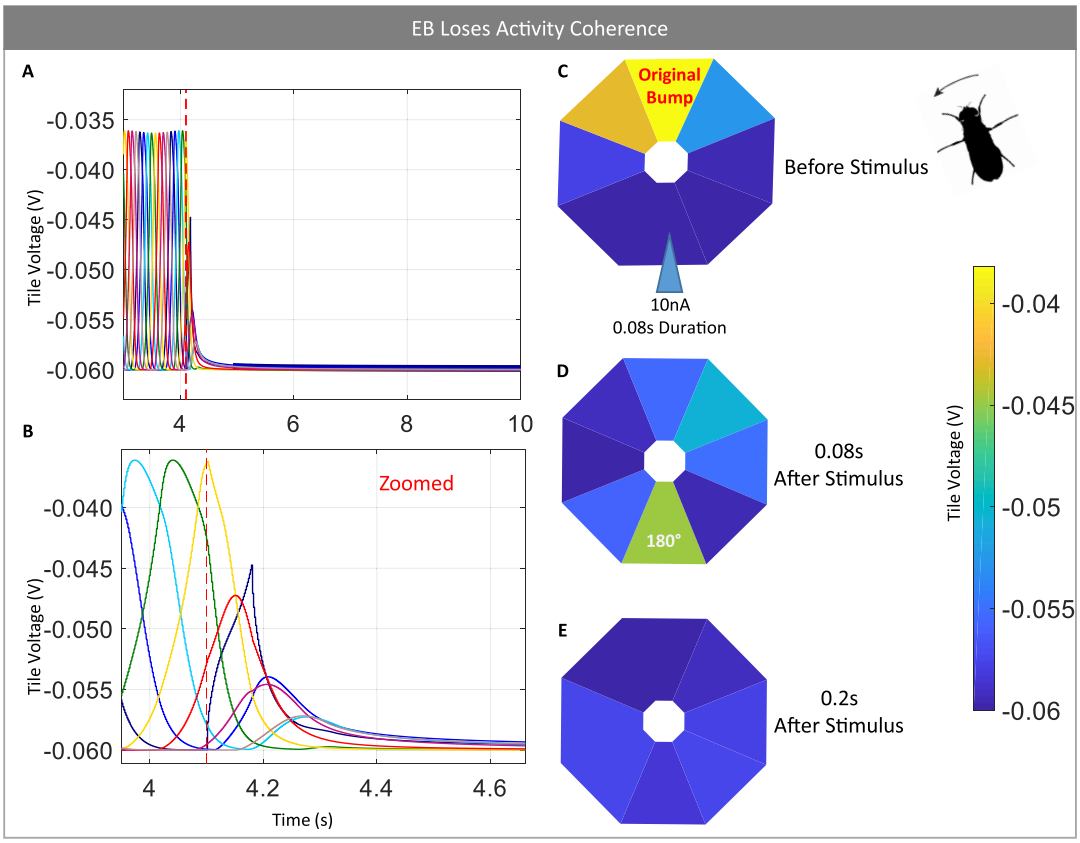

Figure 7. Artificial stimulation applied to the EB was able to disrupt EB bump activity. Just prior to the applied stimulus, the peak bump activity can be seen in tile 5 (C). A stimulation of 10 nA for 0.08 s targeting a 180° offset from the original maximum tile activity caused a loss of EB coherence. At the end of 0.08 s stimulus (D) the bump did jump to the targeted 180° offset but was short lived. 0.02 s following the start of the stimulus, the bump activity is lost, where all tiles of the EB are close to the resting potential (E). The line graphs show the time of stimulation application ($t = 4.10$ s; indicated with dashed, red line) which is deployed at the peak of the tile 5 activity. If the bump jump were to have been successful, maximal activity would quickly move to tile 1. Instead, there is a partial depolarization of tile 1 which causes a partial inhibition of tile 2, both of which are short acting before the EB loses complete coherence.

a chordotonal antennae sensor that provided continuous neuronal signaling to the EB/PB axis of the CX for self-motion tracking. To establish the simulation's merit, we first showed that our *in silico* model was able to emulate the four key experimental observations:

1. The direction of body rotation dictates direction of activity bump in the EB layer.
2. The body's rotational speed correlates to bump activity speed in the EB.
3. The heading, determined by peak bump activity, can be updated with artificial stimulation applied to an EB neuron population, thereby causing a 'bump jump'.
4. A 'bump jump' can be induced through artificial stimulation applied to the PB neuronal populations as well.

Beyond these four experimental behaviors that our model can reproduce, we presented synaptic parameter exploration of the memory and EB internal inhibition synapses as a means to control the dynamics of the EB bump activity. That is, for two or more sensory inputs providing body position, we address here how the CX may compromise between multiple systems during the integration step and determine a single output. Although sensors exhibit adaptive sensitivity [46] and that modality weight determination may be done upstream of the CX [29] (possibly at the sensor level itself), we hypothesize that this weight determination happens in the CX, which is consistent with several studies that have found that many different sensor types converge at the CX, including the halteres [47], antennae [10, 48], and eyes [2, 4, 49].

4.1. Issue with multimodal inputs to same cell populations

Both Green and Kim presented work on artificial stimulations localized in either the EB or PB and showed that these stimulations could update the EB on believed body position while the body was stationary [2, 24]. Our simulation was also able to update believed body position in a stationary body in a similar fashion, so we asked how this direct integration would perform in a rotating body (results section 3.1.3). While the direct integration mechanism did permit orientation updates in a

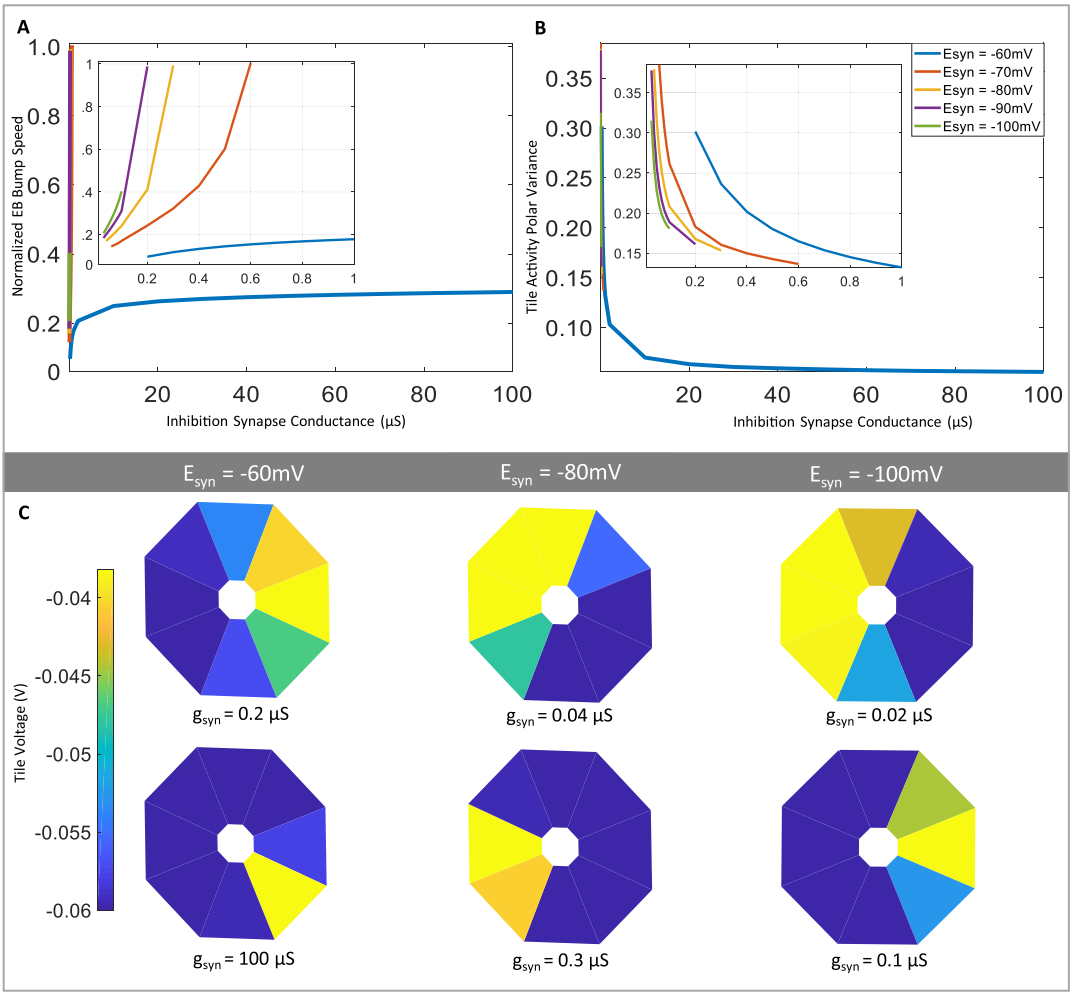

Figure 8. Internal EB inhibition network tuning. (A) Speed of bump activity increases as the synaptic conductance increases. (B) Activity distribution of the EB tiles has an inverse relationship with the synapse conductance, g_{syn}. The reversal potential, E_{syn}, does not appear to alter the variance profiles, however, its value does effect the allowable synaptic conductance values. (c) The upper and lower bounds of g_{syn} permitted for each E_{syn} is shown with the corresponding tile activity map. For an $E_{syn} = -0.06$ V, the functional values of g_{syn} is large, spanning from 0.2 μs–100 μs. Note that in all cases, low g_{syn} causes high variance as seen by multiple tile recruitment during activity (top row), while higher g_{syn} values correspond to lower variance and fewer simultaneous tile activities (bottom row). But in the case of $E_{syn} = -0.06$ V, both high and low variance profiles have a sharper variance profile with a single tile representing maximal activity when compared to higher values of E_{syn}.

moving body, we identified instances of activity loss when the motion-tracking bump activity and the artificial stimulation (i.e. the secondary system input) had destructive interference. These instances tended to occur when the EB was receiving contradictory information from multiple modality inputs. This resulted when the maximal inhibition and the artificial stimulation would coincide in the same tile, causing complete loss of EB electrical activity. With the existing EB inhibition network and with direct integration from a secondary system, this mechanism seems susceptible to problems. The simulated CX experiments performed by Fiore *et al* also showed 'depleted' activity as well, resulting in confused mappings to motor control outputs [29]. Therefore it is unlikely that multiple forms of sensory input converge onto the same layer of the CX in this way—without upstream processing.

4.1.1. Parallel EB ring architecture used to mitigate direct integration

To avoid the potential interferences shown in results section 3.2.1, we propose to use a layered EB approach in our future modeling studies (figure 10). In this layered architecture, a single sensory system will have a dedicated layer in the EB that will independently have a determined body orientation based on that single system's input. This is based on the observation that the EB contains multiple concentric layers, whose exact functions are not known [50]. Once each sensory system has its input represented by bump activity in its corresponding EB layer, the question becomes how to form a single believed heading from these multiple layers. We propose a two step approach that uses (1) an inter-system modulation mechanism followed by (2) a weighted average of bump activity across these parallel rings.

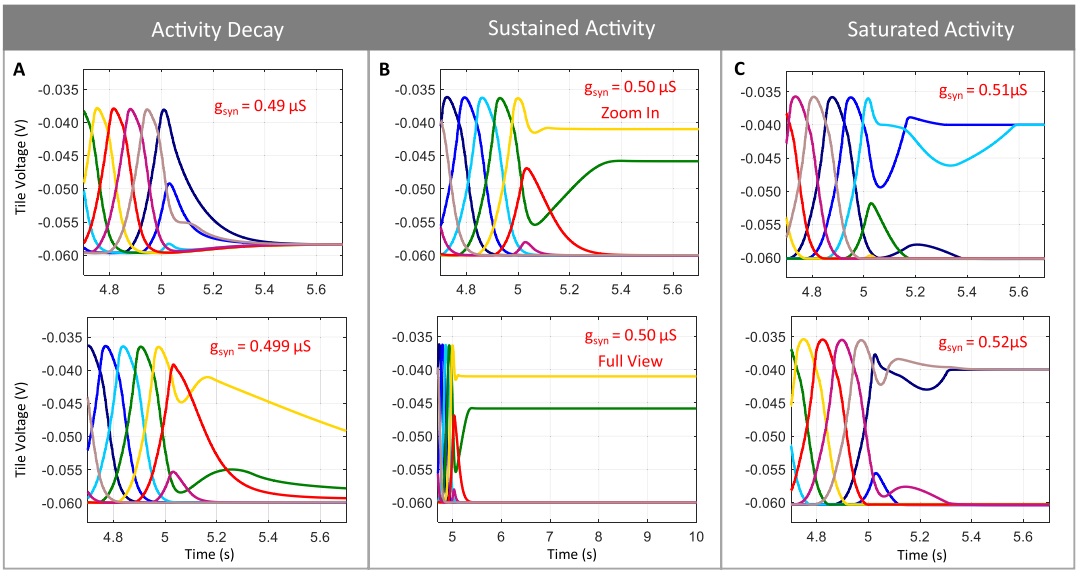

Figure 9. Manipulating memory synapse parameters can alter memory trace profiles. (A)–(C) show changes in the memory traces in a narrow range around the value g_{syn} =0.50 μs which was found to be the stable point to provide sustained memory. (A) and (C) show small deviations from this stable point where (A) shows that a decrease in g_{syn} results in a memory decay and (C) shows that an increase g_{syn} results in memory saturation.

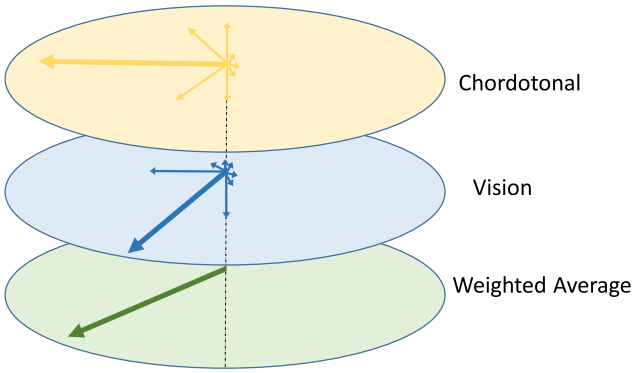

Figure 10. Parallel EB rings. Each layer is dedicated to a single sensory input. The magnitude and variance of the system's input will effect weight of the vote in determining the final body determined from the weighted average step.

4.1.2. How these parallel EB rings might interact

As presented in section 3.2.2, the conductance of the internal inhibitory synapses, g_{syn}, was able to greatly control the variance of the tile activity, where a larger variance signifies less trust in the sensor input. The memory network is another potential mechanism of inter-system control. We found that the presence of the memory cells were absolutely necessary for the oscillatory bump activity seen in the EB and appears to function much like autaptic connections (i.e. self disinhibiting connections) that have been found to be vital to maintain oscillatory network activity in vertebrate models [51–54] and perhaps in *Drosophila* [30]. The memory regimes presented in section 3.2.3 show a range of memory synapse conductances, g_{syn}, that cause memory decay. By controlling the time duration via this plasticity mechanism, a single system's input can be rendered short-lived by modulating the g_{syn} of the corresponding system's memory synapses and reducing the time in which this specific system influence the vote on the final body position determination.

Thus far, we have discussed how a system input may affect the gain of another, but what our paper does not address, however, is how the CX determines *which* input system is most trusted given the current external and internal states. It is at this point that freely behaving animal studies may lend insight into this question. Insulin experiments done by Bertsch and Ritzmann showed that by altering the insulin levels (i.e. the internal state) of a starved, hunting mantid, the animal will exhibit a behavior shift away from hunting [55]. Currently they are exploring where and how in the brain (or ascending commands) the insulin may be acting to cause these shifts in motivation (which may include the CX). This idea of hormonally driven motiv-

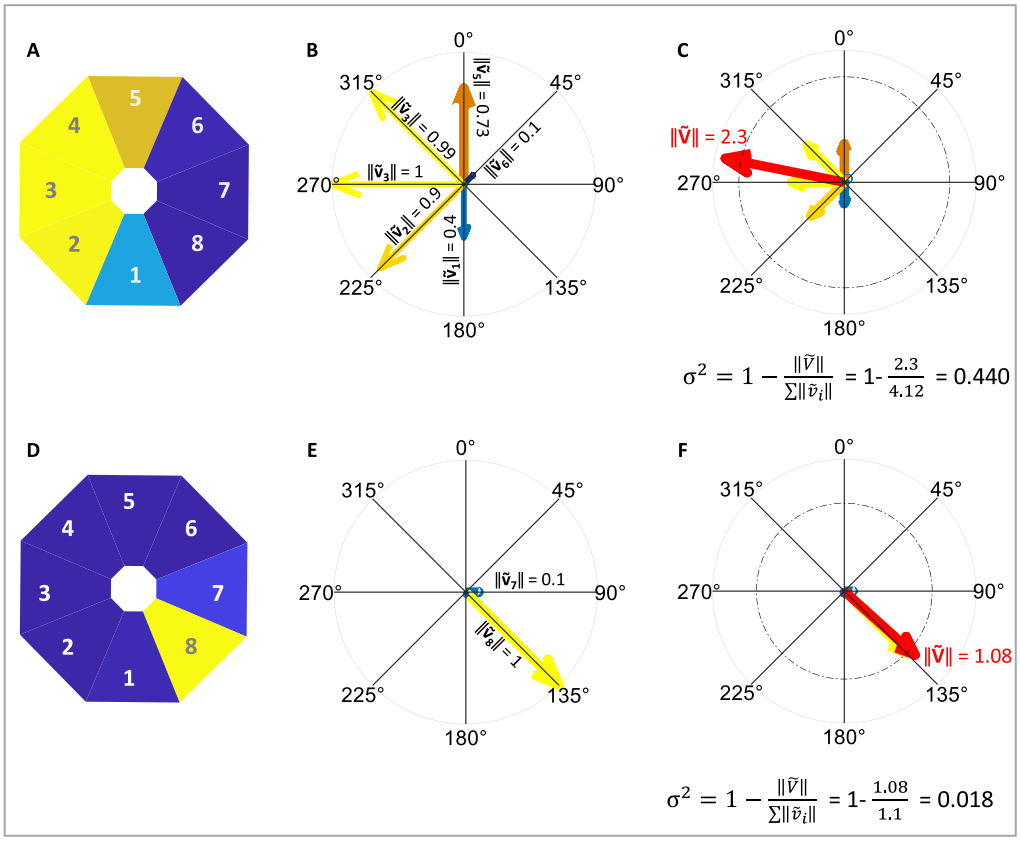

Figure A1. Calculating the variance of time activity across the EB. (A) and (D) Example of high variance tile activity and low variance tile activity, respectively. (B) and (E) Vectorized activity with high and low variance, respectively. (C) and (F) Distribution for high and low variance, respectively.

ations ties well together with the work by Green *et al* [56], where they suggested internal goals are used as a guiding reference to determine moment-to-moment navigational behavior. And like Wystrach *et al*, we hypothesize that system weights are evolutionary determined [32] but fall into contextual regimes. In other words, for a given hormonally dictated motivational state of the animal, sensory inputs will be weighted accordingly.

4.1.3. Tying it all together

In summary, our results support that a simple neuronal architecture can effectively maintain real-time heading updates. This model presents potential mechanisms for adaptive capabilities of the insect nervous system and with it, a better understanding of these situational neuronal behaviors seen in animals [48, 57].

The importance of exploring biological mechanisms of sensory integration is not that biology can perform tasks at speeds outside the capabilities of engineering, but rather we are looking to biology to help us define contextual integration. Although the *same* external stimuli may be detected by the eyes or the antenna, inter-system modulation and integration may differ depending on changes to internal states of the animal. It is this pivotal role of internal states and the resulting changes in CX integration that we are striving to capture. We hope that our model, in conjunction with future work, can be used as a framework for truly adaptive robotic control that can accommodate contextually relevant, complex behavior.

Acknowledgments

This work was supported by the NSF Division of Information and Intelligent Systems, Grant No. 1704366, as well as a GAANN Fellowship.

Appendix. Calculations

A.1. Chordotonal sensor design calculations

This appendix summarizes the parameter calculations for the design of the antennae mass-spring-damper system. These calculations are derived from the equation of motion when no external forces are applied:

$$I\ddot{\theta} + c_t\dot{\theta} + k_t\theta = 0. \tag{A.1}$$

This equation is specific to a rotational mass-spring-damper system where θ is the angle of the mass (i.e. the antenna) relative to the rest angle, I is the moment of inertia of the antenna about the pivot point, C_t is the torsional damping constant, and k_t is the torsional spring stiffness. To relate these torsional elements to the linear elements of the muscles and tendons that support the antennae, we must find

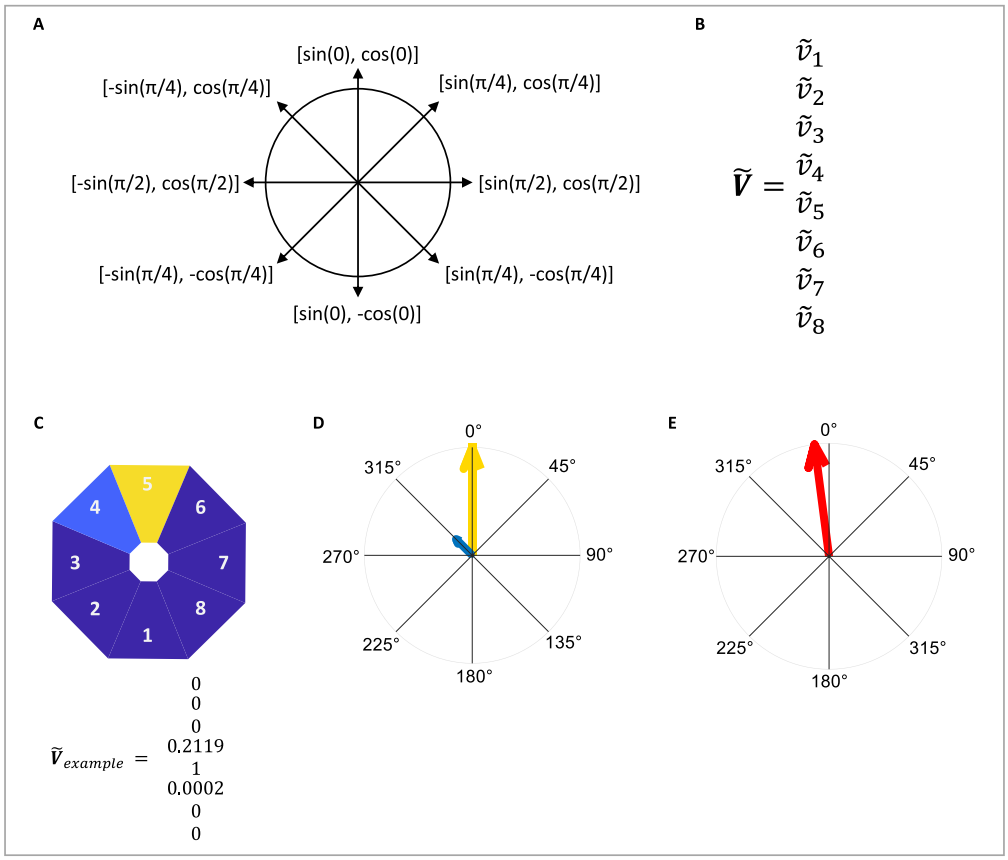

Figure A2. Calculating resultant heading from E-PG voltage values. (A) The unit vectors for each radial position from 0°–360° binned every 45°. (B) E-PG voltages normalized using equation (A.5). (C) Example instance of E-PG normalized activity. Tile five is at maximal activity and is given a weight of one, while tiles four has a fraction of the activity with 0.2119; tile two has a very small weighted activity of 0.0002. (D) The normalized voltage activities presented in (C) are plotted for visual purposes. (E) From vector summation, the resultant vector shows the finalized believed heading.

the *linear* damping constant c, and spring stiffness k. We wish the damping ratio of the system $\zeta = 1$, (i.e. critically damped). With user-defined values of the above variables, the *rotational* damping of the system, c_t, can be transformed to the *linear* damping constant, c, by using equations (A.2)–(A.4). First, the moment of inertia, I, of the antennal flagellum is directly proportional to the length squared and mass,

$$I = \frac{1}{3}mL^2. \tag{A.2}$$

With the moment of inertia defined, the torsional dampening can be calculated.

$$c_t = 2\zeta\sqrt{(k_t I)}. \tag{A.3}$$

Then finally, the linear damping constant can be deduced.

$$c = \frac{c_t}{(\frac{L}{2})^2}. \tag{A.4}$$

A.2. Polar variance calculations

Voltage data was collected from the E-PG neurons of the EB across a time horizon, t.

$$V = \begin{bmatrix} v_1 \\ v_2 \\ v_3 \\ v_4 \\ v_5 \\ v_6 \\ v_7 \\ v_8 \end{bmatrix}$$

Feature scaling was done on voltage data matrix, V, to scale the voltage of each E-PG between 0 and 1:

$$\tilde{V} = \frac{V_i - V_{i,\ min}}{V_{i,\ max} - V_{i,\ min}} = \begin{bmatrix} \tilde{v_1} \\ \tilde{v_2} \\ \tilde{v_3} \\ \tilde{v_4} \\ \tilde{v_5} \\ \tilde{v_6} \\ \tilde{v_7} \\ \tilde{v_8} \end{bmatrix}. \tag{A.5}$$

The scaled voltages were then multiplied by the unit vectors, $\hat{e}$, in an element-wise fashion such that each tile's normalized voltage vector is directed along

its corresponding heading (example polar variance steps shown in figures A1(B) and (E)).

$$\hat{e} = \begin{bmatrix} \sin(0) & \cos(0) \\ \sin(\frac{\pi}{4}) & \cos(\frac{\pi}{4}) \\ \sin(\frac{\pi}{2}) & \cos(\frac{\pi}{2}) \\ \sin(\frac{\pi}{4}) & -\cos(\frac{\pi}{4}) \\ \sin(0) & -\cos(0) \\ -\sin(\frac{\pi}{4}) & -\cos(\frac{\pi}{4}) \\ -\sin(\frac{\pi}{2}) & \cos(\frac{\pi}{2}) \\ -\sin(\frac{\pi}{4}) & \cos(\frac{\pi}{4}) \end{bmatrix}.$$

The normalized tile vectors are then summed to produce the resultant vector (figures A1(C) and (F)). The resultant vector magnitude is divided by the summed normalized tile magnitudes and subtracted from one to produce the polar variance,

$$\sigma^2_{\text{polar}} = 1 - \frac{\|\tilde{\mathbf{V}}_\mathbf{i}\|}{\sum_{n=1}^{8} \tilde{v}_\mathrm{i}}. \tag{A.6}$$

A.3. Believed position calculations

Voltage data was collected from the E-PG neurons of the EB across a time horizon, t. Feature scaling was done as shown in equation (A.5) to scale the voltage of each E-PG between 0 and 1. The scaled voltages were then multiplied by the unit vectors, $\hat{e}$,

$$\hat{e} = \begin{bmatrix} \sin(0) & \cos(0) \\ \sin(\frac{\pi}{4}) & \cos(\frac{\pi}{4}) \\ \sin(\frac{\pi}{2}) & \cos(\frac{\pi}{2}) \\ \sin(\frac{\pi}{4}) & -\cos(\frac{\pi}{4}) \\ \sin(0) & -\cos(0) \\ -\sin(\frac{\pi}{4}) & -\cos(\frac{\pi}{4}) \\ -\sin(\frac{\pi}{2}) & \cos(\frac{\pi}{2}) \\ -\sin(\frac{\pi}{4}) & \cos(\frac{\pi}{4}) \end{bmatrix}$$

which are radially positioned at each 45° bin (figure A2(A)). The scaled voltages were then multiplied element-wise by the unit direction matrix, which results a voltage representation for each tile pointing in its corresponding heading. Figures A2(C)–(E) shows an example of this concept, with figure A2(C) showing the instantaneous activity in the EB, figure A2(D) showing the weighted values of each tile's activity pointed along the tile's heading, and figure A2(E) showing the resultant heading determined by vector addition of figure A2(D).

ORCID iDs

S C Pickard https://orcid.org/0000-0001-5593-9937
N S Szczecinski https://orcid.org/0000-0002-6453-6475

References

[1] Varga A G and Ritzmann R E 2016 *Curr. Biol.* **26** 1816–28
[2] Green J, Adachi A, Shah K K, Hirokawa J D, Magani P S and Maimon G 2017 *Nature* **546** 101–6
[3] Stone T, Webb B, Adden A, Weddig N B, Honkanen A, Templin R, Wcislo W, Scimeca L, Warrant E and Heinze S 2017 *Curr. Biol.* **27** 3069–85
[4] Turner-Evans D, Wegener S, Rouault H, Franconville R, Wolff T, Seelig J D, Druckmann S and Jayaraman V 2017 *eLife* **6** 1–39
[5] Wessnitzer J and Webb B 2006 *Bioinspir. Biomim.* **1** 63–75
[6] Homberg U 2004 *Naturwissenschaften* **91** 199–208
[7] Strausfeld N J and Hirth F 2013 *Science* **340** 157–61
[8] Ito K *et al* 2014 *Neuron* **81** 755–65
[9] Wolff T, Iyer N A and Rubin G M 2015 *J. Comp. Neurol.* **523** 997–1037
[10] Martin J P, Guo P, Mu L, Harley C M and Ritzmann R E 2015 *Curr. Biol.* **25** 2795–803
[11] Homberg U 2008 *Arthropod Struct. Dev.* **37** 347–62
[12] Strauss R 2002 *Curr. Opin. Neurobiol.* **12** 633–8
[13] Strausfeld N J 1999 A brain region in insects that supervises walking *Peripheral and Spinal Mechanisms in the Neural Control of Movement* (Amsterdam: Elsevier Science) vol 123 pp 273–84
[14] Ilius M, Wolf R and Heisenberg M 1994 *J. Neurogenet* **21** 321–38
[15] Strauss R, Hanesch U, Kinkelin M, Wolf R and Heisenberg M 1992 *J. Neurogenet* **8** 125–55
[16] Poeck B, Triphan T, Neuser K and Strauss R 2008 *Dev. Neurobiol.* **68** 1046–58
[17] Neuser K, Triphan T, Mronz M, Poeck B and Strauss R 2008 *Nature* **453** 1244–7
[18] Ridgel A L, Alexander B E and Ritzmann R E 2007 *J. Comp. Physiol.* A **193** 385–402
[19] Harley C M and Ritzmann R E 2010 *J. Exp. Biol.* **213** 2851–64
[20] Honkanen A, Adden A, Da Silva Freitas J and Heinze S 2019 *J. Exp. Biol.* **222** Suppl 1
[21] el Jundi B, Warrant E J, Pfeiffer K and Dacke M 2018 *J. Comp. Neurol.* **526** 2612–30
[22] Seelig J D and Jayaraman V 2015 *Nature* **521** 186–91
[23] Heinze S 2017 *Curr. Biol.* **27** R409–12
[24] Kim S S, Rouault H, Druckmann S and Jayaraman V 2017 *Science* **356** 849–53
[25] Givon L E, Lazar A A and Yeh C H 2017 *Frontiers Behav. Neurosci.* **11** 102
[26] Kakaria K S and de Bivort B L 2017 *Frontiers Behav. Neurosci.* **11** 1–13
[27] Su T S, Lee W J, Huang Y C, Wang C T and Lo C C 2017 *Nat. Commun.* **8** 139
[28] Kottler B *et al* 2017 *BioRxiv* 100420 (at press)
[29] Fiore V G, Kottler B, Gu X and Hirth F 2017 *Frontiers Behav. Neurosci.* **11**
[30] Franconville R, Beron C and Jayaraman V 2018 *eLife* **7**
[31] Goldschmidt D, Manoonpong P and Dasgupta S 2017 *Frontiers Neurorobotics* **11** 1–17
[32] Wystrach A, Mangan M and Webb B 2015 *Proc. R. Soc.* B **282**
[33] Hoinville T and Wehner R 2018 *Proc. Natl Acad. Sci. USA* **115** 2824–9
[34] Cofer D, Cymbalyuk G, Reid J, Zhu Y, Heitler W J and Edwards D H 2010 *J. Neurosci. Methods* **187** 280–8
[35] Mongeau J M, Demir A, Jayaram K, Full R J, Dallmann C J and Cowan N J 2014 *J. Exp. Biol.* **217** 3333–45
[36] Ikeda S, Toh Y, Okamura J Y and Okada J 2004 *Zoolog. Sci.* **21** 375–83
[37] Kavlie R G and Albert J T 2013 *Curr. Biol.* **23** 334–5
[38] Harley C M, English B A and Ritzmann R E 2009 *J. Exp. Biol.* **212** 1463–76
[39] Comer C and Baba Y 2011 *Phil. Trans. R. Soc.* B **366** 3006–15
[40] Toh Y 1981 *J. Ultrasruct. Res.* **77** 119–32
[41] Nishino H, Nishikawa M, Yokohari F and Mizunami M 2005 *J. Comp. Neurol.* **493** 291–308
[42] Patella P and Wilson R I 2018 *Curr. Biol.* **28** 1189–203.e5
[43] Szczecinski N S, Hunt A J and Quinn R D 2017 *Frontiers Neurorobotics* **11** 1–37
[44] Dennis J E and Schnabel R B 1996 *Numerical Methods for Unconstrained Optimization and Nonlinear Equations* (Philadelphia, PA: SIAM)
[45] de Leeuw J 2009 *Wiley Interdiscip. Rev.: Comput. Stat.* **1** 128–9
[46] Borst A, Flanagin V L and Sompolinsky H 2005 *Proc. Natl Acad. Sci.* **102** 6172–6

[47] Kathman N D and Fox J L 2019 *J. Neurosci.* **39** 4100–12
[48] Varga A G, Kathman N D, Martin J P, Guo P and Ritzmann R E 2017 *Frontiers Behav. Neurosci.* **11** 1–4
[49] Seelig J D and Jayaraman V 2013 *Nature* **503** 262–6
[50] Young J M and Armstrong J D 2010 *J. Comp. Neurol.* **518** 1500–24
[51] Fan H, Wang Y, Wang H, Lai Y C and Wang X 2018 *Sci. Rep.* **8** 1–13
[52] Bacci A and Huguenard J R 2006 *Neuron* **49** 119–30
[53] Bekkers J M and Stevens C F 1991 *Proc. Natl Acad. Sci.* **88** 7834–8
[54] Lubke J, Markram H, Frotscher M and Sakmann B 1996 *Ann. Anat.* **178** 309–10
[55] Bertsch D J, Martin J P, Svenson G J and Ritzmann R E 2019 *J. Exp. Biol.* **222** 11
[56] Green J, Vijayan V, Pires P M, Adachi A and Maimon G 2018 *Nat. Neurosci.* **52** 156-164
[57] Ritzmann R E *et al* 2012 *Frontiers Neurosci.* **6** 1–10